Analysis of the influence of stress triaxiality on formability of hole-flanging by single-stage SPIF

A. J. Martínez-Donaire*, M. Borrego, D. Morales-Palma, G. Centeno, C. Vallellano

[1] Department of Mechanical and Manufacturing Engineering, Higher Technical School of Engineering, University of Seville, 41092, Seville, Spain

***** Corresponding author: ajmd@us.es; Tel.: +34-954-487311

Abstract

Traditionally the fracture in sheet metal forming is characterized by the fracture forming limit (FFL) curve typically obtained by using conventional Nakajima tests. This curve is implicitly assumed a material property. Single point incremental forming (SPIF) is a novel and flexible forming process characterized by the ability to suppress local necking and develop stable plastic deformation up to sheet fracture. In many cases, these fracture strains are clearly above the conventional FFL. The current work presents a numerical study of the evolution of stress triaxiality in SPIF in the $\bar{\varepsilon} - \bar{\eta}$ space. The simulations are validated with hole-flanging tests by single-stage SPIF over AA7075-O sheet of 1.6 mm thickness. The difference in the average stress triaxiality at fracture exhibited in SPIF and Nakajima tests would allow explaining the enhancement on formability observed in incremental sheet forming.

Keywords: Single point incremental forming (SPIF); Hole-flanging; Stress triaxiality; Formability; Fracture forming limit (FFL)

1. Introduction

Single Point Incremental Forming (SPIF) is a novel and flexible forming technology that has been used in the last few years to obtain a variety of customized sheet parts [1]. One of the most valuable advantages of this process is its ability to generate a stable plastic deformation up to the ductile fracture of the sheet [2]. As a consequence, the safe forming region enlarges notably compared with that in conventional stamping processes, which are limited by local necking.

Traditionally, the fracture in sheet metal forming processes is characterized by the fracture forming limit (FFL) curve. This fracture locus comprises tensile cracks, i.e. mode I cracks of fracture mechanics [3], spreading from uniaxial to equibiaxial tension condition in the forming limit diagram (FLD). The FFL, typically obtained by using conventional Nakajima or Marziniak

tests, is implicitly assumed to be a material property. However, there are no definitive evidences backing such hypothesis.

There is number of studies in the literature showing values of fracture strains in SPIF compatible with the conventional FFL for some materials, within a reasonably experimental scatter. For instance, this is pointed out in aluminium alloy AA1050-H111 sheets with 1 mm thickness in SPIF tests of truncated conical and pyramidal shapes [2,4] and cylindrical flanges [5], and in sheets of titanium (grade 2) alloy sheet with 0.7 mm thickness [5] and AISI 304L stainless steel with 0.5 mm thickness [6] in tests of cylindrical hole-flanging by SPIF. However, there are also investigations where SPIF processes exhibit fracture strains values clearly above the conventional FFL, providing an unexpected gain of formability in some materials. Centeno et al. [7,8] analysed the spifability of AISI 304 sheets 0.8 mm thickness performing conical frustum shapes. They found that fracture strains in SPIF were located clearly above the conventional FFL, concluding that Nakajima tests were not suitable to evaluate the FFL for SPIF in this case. Furthermore, this significant enhancement of formability could not be explained only by the bending induced by the tool, pointing out that the sensitivity of the material to the triaxiality state should be taking into account to understand the fracture process. Haque and Yoon [9] studied experimental and numerically the formability and failure in SPIF of cone and pyramidal shapes of aluminium alloy AA 6022-T4E32 sheet of 1 mm thickness. For both shapes, the principal strain distribution showed values exceeding both the necking and fracture limit. A similar behaviour was found by Borrego et al. [10] in the hole-flanging process by single-stage SPIF in aluminium alloy AA7075-O sheet of 1.6 mm thickness. More recently, Mirnia and Shamsari [11] have presented a detailed numerical and experimental analysis of fracture in SPIF of the AA6061-T6 aluminium alloy sheet with 1 mm thickness using truncated pyramids and cones, and straight grooves. By comparing the fracture strains obtained under a proportional loading tests and under highly nonlinear loading as in SPIF tests, they found rather different fracture curves for both cases. They concluded that the FFL is strongly dependent on the loading path, showing that the severely non-proportional loading and cycling strain paths result in raising the fracture limit in SPIF compared to conventional processes with proportional loading.

The stress triaxiality is, besides the strain level, probably the most important factor that affects formability at fracture in a forming process [12,13]. The stress triaxiality, defined as the ratio of the mean or hydrostatic stress (σ_m) and equivalent stress ($\bar{\sigma}$), i.e. $\eta = \sigma_m/\bar{\sigma}$, controls the micro-void growth phase during ductile fracture [14-16]. Thus, low level of triaxiality prevents voids to growth, postponing the final fracture and causing an apparent enhancement in formability [16,17]. According to this, differences in triaxiality levels could justify the experimental differences observed in the FFL obtained by conventional (e.g. Nakajima) and incremental (e.g. SPIF) tests.

The aim of this article is to offer a critical discussion about the influence of the stress triaxiality in the onset of ductile fracture in incremental sheet forming processes, contributing to improve the current level of understanding on the material formability in this innovative flexible technology. A numerical analysis of the evolution of stress triaxiality in a hole-flanging process by single-stage SPIF is developed, and validated with experimental results in AA7075-O sheet of 1.6 mm thickness. The features of the local stress triaxiality, average stress triaxiality and accumulated equivalent plastic strain in both sides of the sheet at the fracture site are discussed. The analytical mapping of the conventional FFL from the $\varepsilon_1 - \varepsilon_2$ space to the $\bar{\varepsilon} - \bar{\eta}$ space assuming a simplified kinked strain in Nakajima tests is presented. The differences in the average stress triaxiality value at fracture exhibited in SPIF and Nakajima tests in the $\bar{\varepsilon} - \bar{\eta}$ space might explain the enhancement on formability observed in incremental sheet forming.

2. Experimental tests

A detailed description of the material characterization procedure and SPIF tests can be found in [10]. The material studied was an aluminum alloy 7075-O, supplied as a sheet of 1.6mm thickness. Table 1 summarizes the elastic/plastic parameters and Lankford coefficients for this material. The plastic stress-strain curve is fitted using a power-law (Hollomon-type law) as

$$\bar{\sigma}(MPa) = 300\ \bar{\varepsilon}_p^{0.12}, \tag{1}$$

where $\bar{\sigma}$ ad $\bar{\varepsilon}_p$ are the equivalent stress and equivalent plastic strain respectively. Figure 1(a) depicts the FLC and FFL experimentally obtained using Nakajima tests.

A series of hole-flanging experiments by single-stage SPIF were carried out over specimens with different milled holes (pre-cut hole, d_0) in the center. The inner diameter of the final flanged hole (d_f) was 95.8 mm. A schema of the process is depicted in Figure 1(b). The step down was set to 0.2 mm/rev. Two hemi-spherical forming tools of ϕ12 and ϕ20 mm diameter were used.

Table 1. Elastic/plastic properties and normal anisotropy (average values: $(x_0 + 2x_{45} + x_{90})/4$), and Lankford coefficients for AA7075-O with 1.6mm thickness [10]

E [GPa]	ν	YS [MPa]	UTS [MPa]	r	r_0	r_{45}	r_{90}
62.5	0.3	109.5	214	0.85	0.65	0.97	0.81

Experiments were conducted on a 3-axis milling CNC machine EMCO VMC-200. The toolpaths were developed in CATIA V5, following a combination of z-level and cylindrical helical trajectories (see virtual trajectories in Figure 1(b)). Finally, the principal strains at the outer (no contact with the forming tool) surface of the flanged specimens were evaluated using photogrammetry via the 3D optical measurement system ARGUS®.

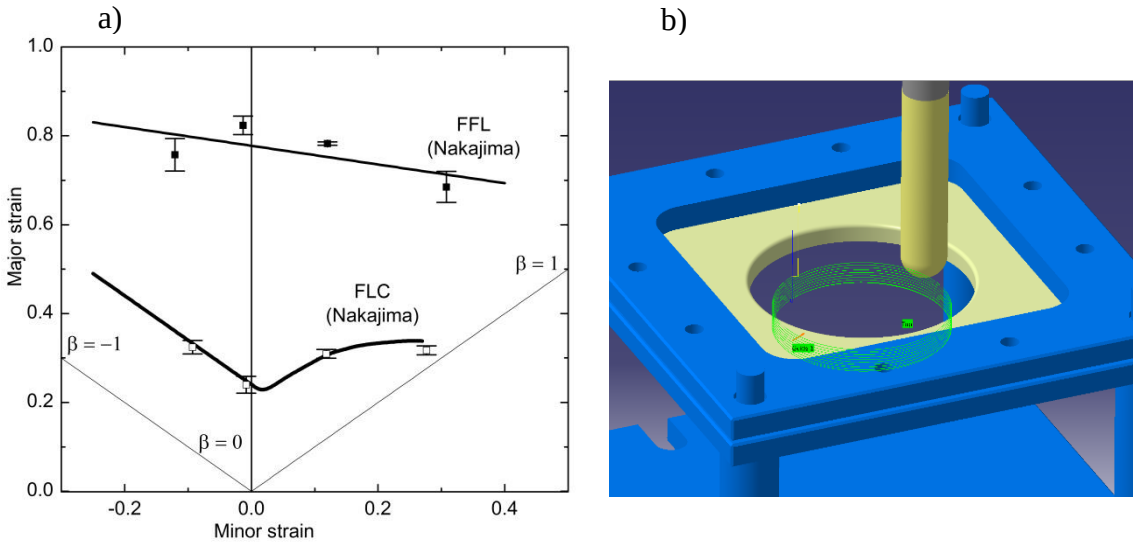

Figure 1. FLC and FFL in the $\varepsilon_1 - \varepsilon_2$ space for AA7075-O sheet 1.6 mm thickness (a). Screenshot of tool trajectories generated in CATIA V5 for hole flanging operation by single-stage SPIF (b).

Table 2. Results of hole flanging by single-stage SPIF with pre-cut holes ranging from 70 to 55 mm diameters and tools of ϕ12 and ϕ20 mm. Successful flanges (S) and failed flanges (F). The experimental major and minor fracture strain values are shown ($\varepsilon_1^f : \varepsilon_2^f$).

Tool diameter	**Pre-cut hole diameter (mm)**							
	55	**56**	**58**	**61**	**62.5**	**63.5**	**65**	**70**
12 mm					F	**F**	**S**	S
($\varepsilon_1^f : \varepsilon_2^f$)						(0.851 : 0.097)		
20 mm	F	**F**	**S**	S				
($\varepsilon_1^f : \varepsilon_2^f$)		(0.875 : 0.120)						

Table 2 summarizes the experiments performed with both tools and different pre-cut holes ranging from 70 to 55 mm diameters. The legend "F" indicates fractured specimen, while "S" means successful test, i.e. a tests in which a satisfactorily flanged part was obtained. As can be seen, the limit of formability in terms of initial pre-cut hole is between 63.5 mm and 65 mm diameter for ϕ12mm forming tool, and between 56 mm and 58 mm diameter for the tool of ϕ20mm. The experimental major and minor fracture strains ($\varepsilon_1^f : \varepsilon_2^f$) for flanges of ϕ63.5 and ϕ56 mm precut holes and ϕ12 and ϕ20 mm tools respectively are shown. Figure 2 depicts the pair of specimens in this latter case and the evolution of the major and minor principal strains along the flange in the FLD in both specimens. As can be seen, the specimen with pre-cut hole

of 56 mm diameter exhibited strain values higher than the FFL curve, as an indicative of the appearance of fracture in the flange, while in the case the successful flange of 58 mm pre-cut hole, the strains were substantially below the FFL.

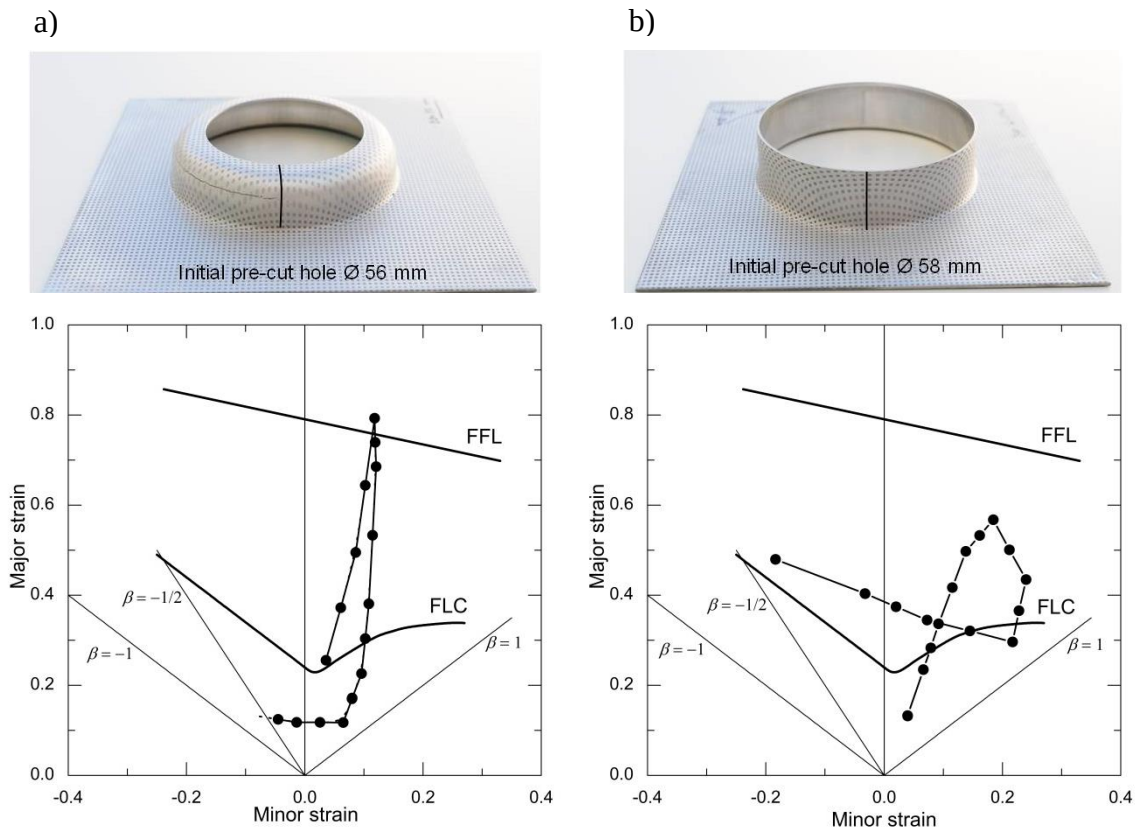

Figure 2. Hole flanging tests with pre-cut holes 56 mm (a) and 58 mm (b) diameter respectively and tool of ϕ20mm. Specimen pictures (top). Evolution of principal strains along the flange in the fractured and successful specimens (down).

3. Numerical Simulation

A numerical model of the incremental hole flanging process is mandatory to carry out the analysis of stress triaxiality on the sheet fracture. The aim of the numerical model is to accurately reproduce the strain and stress evolutions controlling the failure in the sheet.

An explicit dynamic simulation of the hole-flanging operation by single-stage SPIF was performed using LS-Dyna for ANSYS™ software. Figure 3 depicts the finite element mesh and the boundary condition around the perimeter of the sheet (pinned nodes) simulating the blankholder clamping. A full model of the sheet is used, owing to the lack of symmetry in the toolpaths.

The metal sheet was meshed using 4-node shell elements (SHELL 163) with Belytschko-Tsay formulation, reduced integration and hourglassing control. Five integration points across the sheet thickness were selected. The tools and the backing plate were assumed to be rigid bodies.

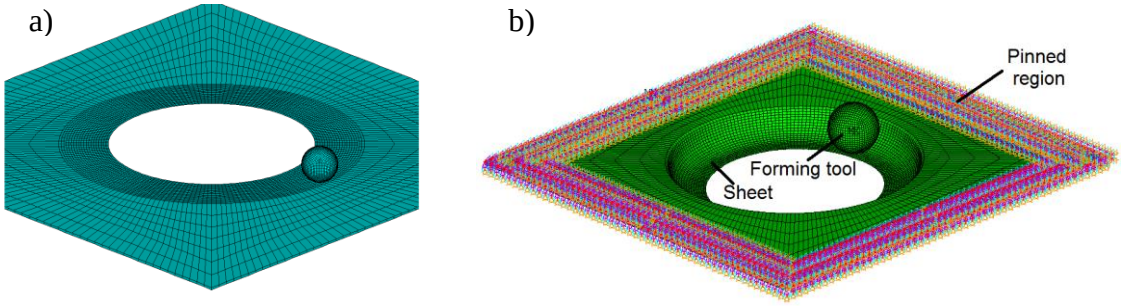

Figure 3. Detail of the finite element mesh in the metal sheet (original configuration) (a) and boundary condition in the blank-holder region (deformed part) (b).

An elastic-plastic rate-independent material behavior was assumed in the metal sheet. Following the recommendations for aluminum alloys, a Barlat and Lian anisotropic yielding criterion [18] with exponent $m = 8$ was used. The mechanical properties are given in section 2.

Regarding the contact conditions, a Coulomb's friction law with a friction coefficient of $\mu = 0.15$ for both tool-sheet and backing plate-sheet contacts was assumed.

3.1. Validation of the numerical model

The validation of the model is focused on reproducing the strains on the flange at the failure location. Thus, it is assumed that the more realistic the simulated strains, the more accurate the stress evolution and, therefore, the better the triaxiality predictions.

To this end, a series of virtual hole flanging operations by single-stage SPIF were run with pre-cut hole diameters given in Table 2 and both ϕ12 and ϕ20 mm tool. As in experimental tests, the failure by fracture was numerically predicted when the major strain at some point of the outer side of the flange reached the major strain at fracture measured in the corresponding experimental SPIF test.

Table 3. Numerical predictions vs. experimental results of hole flanging by single-stage SPIF. Failed (F) and successful (S) flanges.

Tool diameter	**Results**	**Pre-cut hole diameter (mm)**										**LFR**
		55	**56**	**58**	**61**	**62.5**	**63.5**	**65**	**67**	**68**	**70**	
12 mm	FEA						F	**F**	**S**	S		1.43
	Exp.					F	**F**	**S**			S	1.47
20 mm	FEA	F	**F**	**S**		S						1.65
	Exp.	F	**F**	**S**	S							1.65

Following the above criterion, Table 3 shows the numerical predictions of failed (F) and successful (S) flanges in comparison with the experimental results. As can be seen, the

predicted numerical failure is associated with initial holes of ϕ65 and ϕ56 mm for tools of ϕ12 and ϕ20 mm, respectively. Their corresponding experimentally obtained pre-cut holes were ϕ63.5 and ϕ56 mm. The prediction for the ϕ20 mm forming tool matches very well the experimental data whereas there is a slight offset between the numerical and experimental results for the ϕ12 mm tool. This offset may be related, among others, with the unavoidable deviations between the mathematical modelling of the material plastic behaviour and the real one, and the intrinsic inaccuracy of explicit analysis when dealing with elastic-plastic problems with intense contact. It should be mentioned that the results presented here were the best predictions obtained after performing a sensitivity study with the more relevant material parameters, mesh size and element type.

The limiting forming ratio (LFR) values, defined as the ratio of the final diameter and the smallest pre-cut hole diameter that allow obtaining a successful flange, are also displays in Table 3. This parameter is typically used to evaluate the material formability in conventional circular hole-flanging operations. A reasonably good agreement with the experimental results is found.

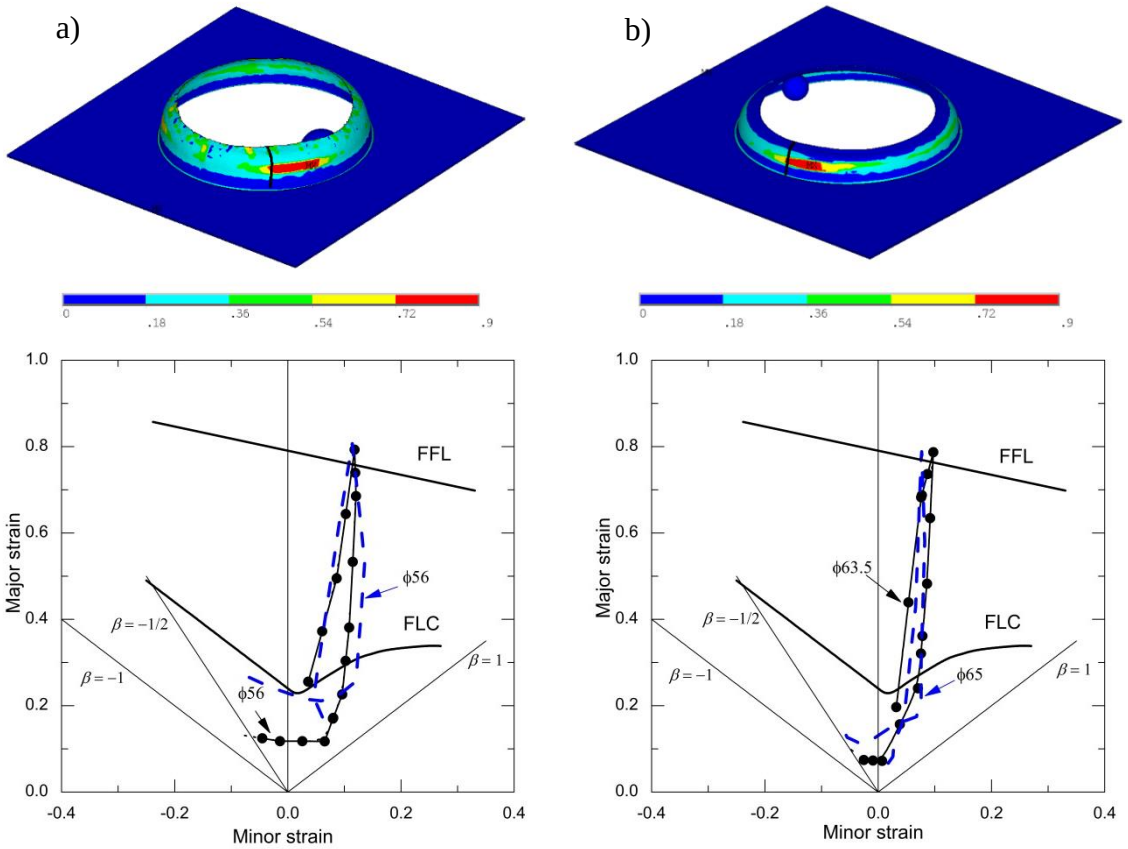

Figure 4. Numerical (blue dash line) principal strains along the failed flanges predicted using ϕ20 mm (a) and ϕ12 mm (b) forming tool versus the experimental flanges. Pre-cut holes of 56 and 65 mm (numerical) versus 56 and 63.5 mm (experimental) respectively. Major strain contours at the outer surface of the sheet for the numerical simulations (top).

Figures 4(a) and 4(b) (top) show the colourmaps of major principal strains at the outer face of the flange for the simulations of ϕ65 and ϕ56 mm precut holes with ϕ12 and ϕ20 mm tools respectively. The predicted location of fracture is assumed to be the zone of higher values of major principal strain, which agrees quite well with their experimental counterpart (see [10]).

Figures 4(a) and 4(b) (bottom) compare the evolution of the numerical (blue dash line) and experimental (black dot line) strains in the FLD in both cases. As in the real tests, the numerical strains are obtained at the outer face of the flange along a path right next to the fracture location (see black line in colourmaps). As can be seen, both shape and level of the strain are in reasonably good agreement with the experimental evidence for both tools.

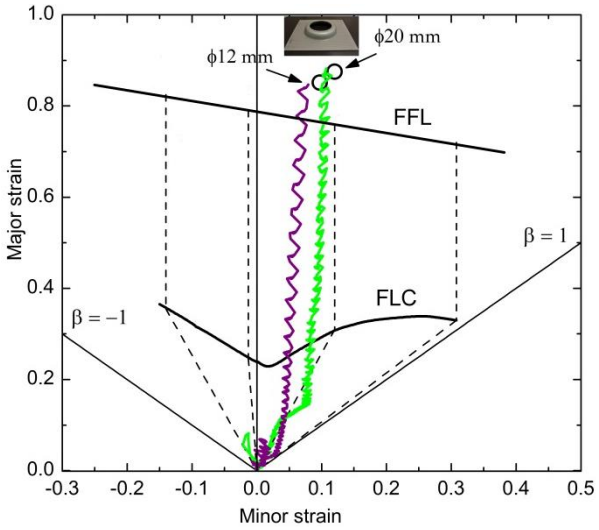

Figure 5. Simulated strain paths at the outer side of the sheet and the predicted fracture site during the hole-flanging operation by single-stage SPIF using ϕ20 and ϕ12 mm forming tools.

Figure 5 depicts the numerical strain evolutions in the limit flanges of both tools within the FLD. The numerical strains are here obtained at the right fracture site predicted numerically and at the outer side of the sheet. The experimental fracture strains are also displayed for comparison (black circles). Two expected facts are here visible. On the one hand, the intense cyclic and non-linear strain path caused by the successive tool passes. On the other hand, the good agreement between the numerical and the experimental fracture strains, which are again clearly above the conventional FFL.

According to the above, the numerical strain evolutions along the flange are quite approximated to the experimental ones in the fractured specimens. As a result, it seems reasonable to assume that the evolution of other local variables, such as effective stress, hydrostatic stress, etc., will also evolve reasonably similar to the real ones. In this sense, the current numerical model can be considered validated for the purpose of this work, that is, to analyze the influence of stress triaxiality on fracture of an incrementally deformed sheet.

4. Stress triaxiality analysis and discussion

As mentioned in the introduction, stress triaxiality is one of the main factors that affects formability formability in a forming process. In this section, the evolution of the local and average stress triaxiality at the fracture initiation point in a hole-flanging process by single-stage SPIF is analysed. The differences in the average stress triaxiality value at fracture exhibited in SPIF and Nakajima tests, and their influence on formability, are discussed in the $\bar{\varepsilon} - \bar{\eta}$ space.

4.1. Local stress triaxiality

Figure 6(a) depicts the numerical stress triaxiality versus the z-displacement of the tool at the element located at fracture site for the limit flange with ϕ20 mm tool. The evolution at the outer and inner surface of the flange in the entire test is displayed.

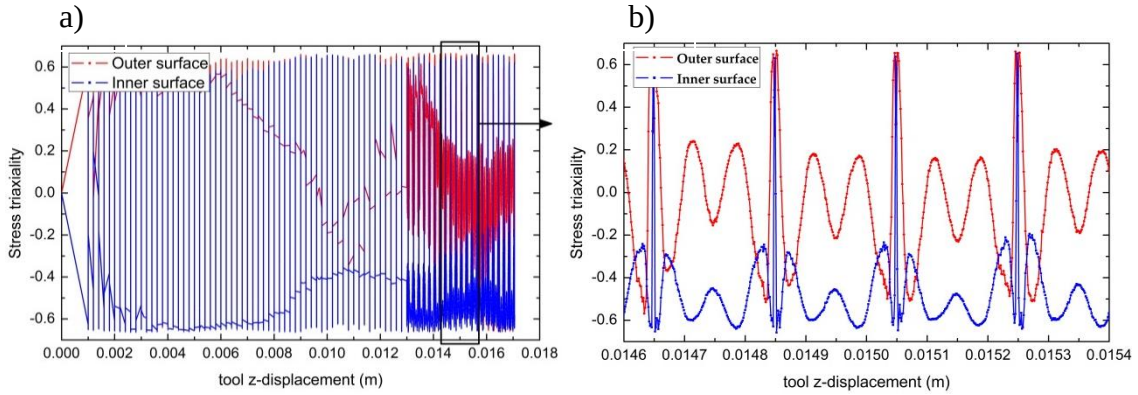

Figure 6. Stress triaxiality vs z-displacement at the inner and outer surface during a hole-flanging process by single-stage SPIF using ϕ20 mm forming tool. Entire test (a) and detail (b).

As can be seen, the stress triaxiality exhibits the typical oscillations related to the successive passages of the tool through the meridian that intersects the considered element. The maximum and minimum values range within 0.66 to -0.66. These values are related with the shape of the alternating strain path shown in Figure 5, in which the local strain ratio ($\beta = d\varepsilon_2/d\varepsilon_1$) is changing alternatively from near equibiaxial stretching to near equibiaxial compression. It should be noted that, for an ideal isotropic sheet, the triaxiality ratio associated to a proportional loading in equibiaxial stretching ($\beta = 1$ in the 1st quadrant) is 0.66 and in equibiaxial compression ($\beta = 1$ in the 3rd quadrant) is -0.66. This agrees with the analysis of Mirnia and Shamsari [11].

These oscillations are better appreciated in the zoom depicted in Figure 6(b). As observed, both outer and inner surfaces show positive and negative peaks. The evolution of stress triaxiality between these peaks is mainly due to the elastic deformation of the flange when the tool is far from the considered element. This fact can be better appreciated in Figure 7, which

depicts the numerical evolution of the equivalent plastic strain vs. the z-displacement of the tool. As can be seen, this increases stepwise up to fracture at both the outer and inner surface (see zoom in the right hand side), remaining constant between tool passages, indicating that only elastic deformation takes place at the considered point. Similar evolution has been experimental and numerically observed by Fang et al. [19] in tests of truncated cone by SPIF. As seen, the outer surface accumulates more equivalent plastic strain than the inner one, showing the existence of a significant strain gradient through the sheet thickness. As pointed out by Morales et al. [20,21] the existence of stress and strain gradients induced by forming tools is the main mechanism to postpone or even suppress local necking in processes involving stretch-bending in the sheet. This fact has been also corroborated in SPIF by Fang et al. [19] and Seong et al. [22].

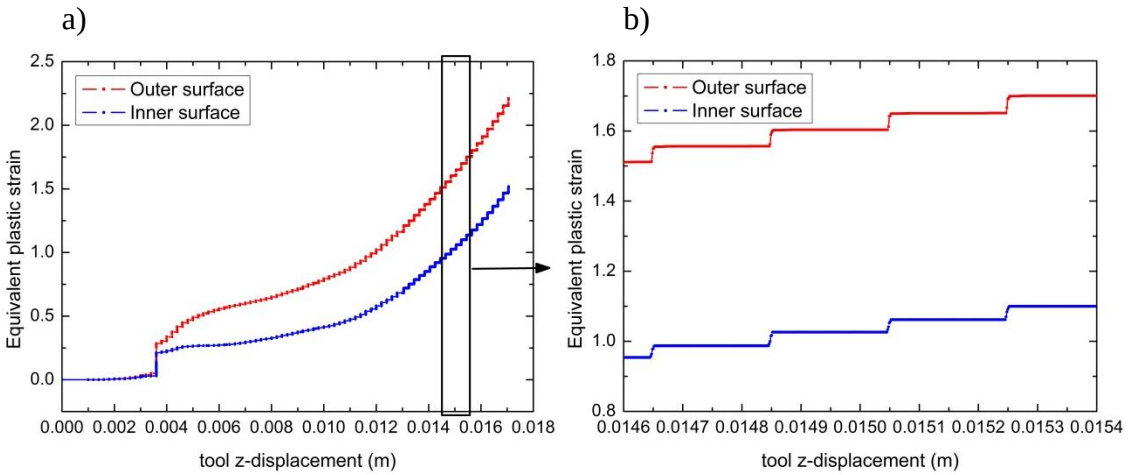

Figure 7. Equivalent plastic strain vs z-displacement at the inner and outer surface during a hole-flanging process by single-stage SPIF using ϕ20 mm forming tool. Entire test (a) and detail (b).

According to the above, it can be concluded that local stress triaxiality at the fracture point seems to evolve with higher mean values at the outer surface than at the inner one. However, due to the incremental deformation, this remains in the elastic regime most of the time, i.e. when the tool is far from this point. It can be assumed that no damage is accumulated in the material during these periods. An identical trend is also observed for the ϕ12 mm tool.

4.2. Average stress triaxiality

In order to quantify the stress triaxiality during the entire process of hole flanging, the average stress triaxiality to fracture ($\bar{\eta}_f$) defined by Bao and Wierzbicki [14] is used, that is,

$$\bar{\eta}_f := \frac{1}{\bar{\varepsilon}_f}\int_0^{\bar{\varepsilon}_f} \frac{\sigma_m}{\bar{\sigma}}\, d\bar{\varepsilon} \tag{3}$$

where $\bar{\varepsilon}$ is the equivalent plastic strain and $\bar{\varepsilon}_f$ is the equivalent plastic strain to fracture. Thus, the average stress triaxiality ($\bar{\eta}$) to a given deformation, can be defined as

$$\bar{\eta} := \frac{1}{\bar{\varepsilon}} \int_0^{\bar{\varepsilon}} \frac{\sigma_m}{\bar{\sigma}} \, d\bar{\varepsilon} \tag{4}$$

According to the original work of McClintock [12], the integral of Eq. (4) can be used as a measured of the accumulated damage by microvoid growth [3,23].

$$D_{void} = \int_0^{\bar{\varepsilon}} \frac{\sigma_m}{\bar{\sigma}} \, d\bar{\varepsilon} = \bar{\eta} \cdot \bar{\varepsilon} \tag{5}$$

Thus, if the mechanisms of microvoid nucleation and coalescence can be neglected, it is stablished that ductile fracture occurs when the accumulated damage by microvoid growth reaches a critical value, that is,

$$\int_0^{\bar{\varepsilon}_f} \frac{\sigma_m}{\bar{\sigma}} \, d\bar{\varepsilon} \equiv D_{crit} \quad \rightarrow \quad \bar{\eta}_f \cdot \bar{\varepsilon}_f \equiv D_{crit} \tag{6}$$

This assumption has been widely used in literature to model ductile fracture in SPIF [3], assuming implicitly that microvoid growth is the more relevant mechanism in the onset of ductile fracture in incremental sheet forming processes.

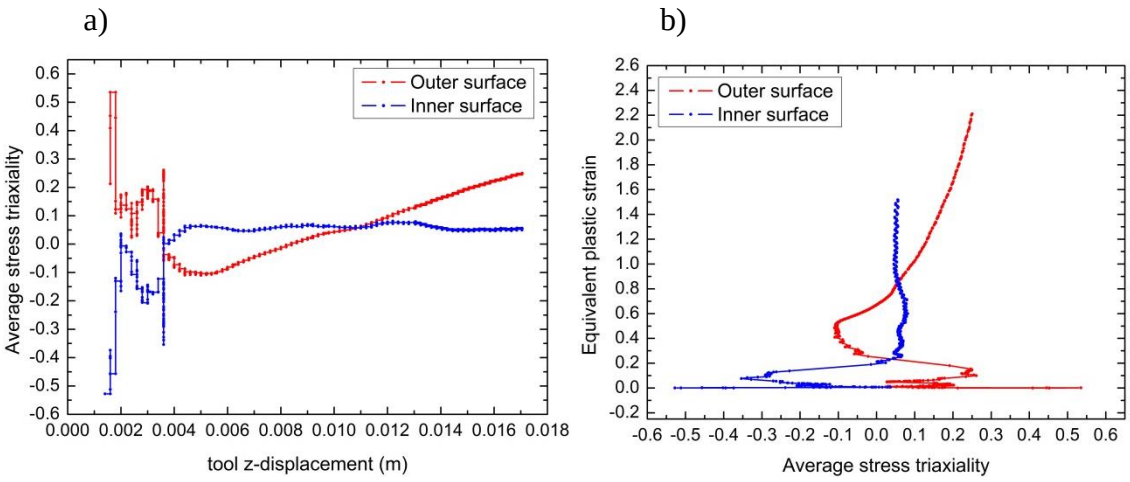

Figure 8. Evolution of average stress triaxiality vs z-displacement (a) and equivalent plastic strain vs. average stress triaxiality (b) at the inner and outer surface during a hole-flanging process by single-stage SPIF using ϕ20 mm forming tool.

Figure 8(a) shows, for the limit flange with ϕ20 mm tool, the average stress triaxiality (Eq. 4) versus the z-displacement of the tool at the element located at fracture site. The evolution at the outer and inner surface is presented. It is observed an initial period with high numerical scatter, mainly due to numerical zero or near zero values of the equivalent stress (see Figure 7). After this, the average stress triaxiality at the outer surface shows a period of negative values until reaching a minimum and increasing hereafter up to fracture. This minimum is related with

the instant in which the forming tool approaches the considered element. The inner surface shows positive values up to fracture. The gradient of $\bar{\eta}$ through the sheet thickness is evident.

Figure 8(b) depicts the evolution of the average stress triaxiality ($\bar{\eta}_f$) and the equivalent plastic strain ($\bar{\varepsilon}_f$) to fracture at fracture point at both sides of the sheet in the $\bar{\varepsilon} - \bar{\eta}$ diagram. It can be clearly appreciated that both $\bar{\eta}_f$ and $\bar{\varepsilon}_f$ at the outer surface are higher than at the inner one. This means that the outer surface exhibits less resistance to accumulate damage by microvoid growth, which assists the triggering of fracture. As before, the same trend is observed for the ϕ12 mm tool.

To elucidate the differences in stress triaxiality between incremental deformation and conventional forming, in the following, both the hole flanging by single-stage SPIF and Nakajima tests are compared in the $\bar{\varepsilon} - \bar{\eta}$ diagram. Hereafter, the analysis will focus on the outer surface as the one controlling the initiation of fracture.

4.3. Nakajima tests in $\bar{\varepsilon} - \bar{\eta}$ space

The mapping of the FFL from the $\varepsilon_1 - \varepsilon_2$ space to the $\bar{\varepsilon} - \bar{\eta}$ space can be done only numerically or analytically. To be mathematically rigorous, the Nakajima tests should be numerically simulated up to fracture reproducing the plastic instability associated to necking in this case. For the purpose of this work, this numerical analysis would provide only mathematical complexity and not better conclusions than performing an approximate analytical mapping. To this end, the constitutive equations associated to Hill's 48 anisotropic yield criterion are used in this section.

It is well known that, when necking occurs in a Nakajima tests, the principal strains in $\varepsilon_1 - \varepsilon_2$ space exhibit a kinked paths. These can be simplified as piecewise linear paths, involving an initial path with a given strain ratio $\beta = d\varepsilon_2/d\varepsilon_1$ up to necking and a local plane strain path after necking to fracture (see schematic paths in Figure 5). Thus, the integrals in the equivalent plastic strain to fracture ($\bar{\varepsilon}_f$) and the average stress triaxiality to fracture ($\bar{\eta}_f$) must be split into two parts

$$\bar{\varepsilon}_f = \int_0^{\bar{\varepsilon}_f} d\bar{\varepsilon} = \int_0^{\bar{\varepsilon}_n} d\bar{\varepsilon} + \int_{\bar{\varepsilon}_n}^{\bar{\varepsilon}_f} d\bar{\varepsilon} \tag{7}$$

$$\bar{\eta}_f = \frac{1}{\bar{\varepsilon}_f}\int_0^{\bar{\varepsilon}_f} \frac{\sigma_m}{\bar{\sigma}}\, d\bar{\varepsilon} = \frac{1}{\bar{\varepsilon}_f}\left[\int_0^{\bar{\varepsilon}_n} \frac{\sigma_m}{\bar{\sigma}}\, d\bar{\varepsilon} + \int_{\bar{\varepsilon}_n}^{\bar{\varepsilon}_f} \frac{\sigma_m}{\bar{\sigma}}\, d\bar{\varepsilon}\right] \tag{8}$$

where subscript n stands for variables at necking. This integration procedure, before and after necking, was suggested originally by Atkins [23] and recently by Sheng [24] to analyze the critical damage at fracture. Using the Hill's 48 yield criterion, the Eq. (7) and (8) are rewrite as follows:

$$\bar{\varepsilon}_f = \int_0^{\varepsilon_{1n}} \frac{d\bar{\varepsilon}}{d\varepsilon_1}\, d\varepsilon_1 + \int_{\varepsilon_{1n}}^{\varepsilon_{1f}} \frac{d\bar{\varepsilon}}{d\varepsilon_1}\, d\varepsilon_1 =$$
$$= \frac{1+r}{\sqrt{1+2r}}\left[\int_0^{\varepsilon_{1n}} \sqrt{1+(2r/(1+r))\beta+\beta^2}\, d\varepsilon_1 + \int_{\varepsilon_{1n}}^{\varepsilon_{1f}} \sqrt{1+(2r/(1+r))\beta_{n-f}+\beta_{n-f}^2}\, d\varepsilon_1\right] \tag{9}$$

$$\bar{\eta}_f = \frac{1}{\bar{\varepsilon}_f}\left[\int_0^{\varepsilon_{1n}} \frac{\sigma_m}{\sigma_1}\frac{\sigma_1}{\bar{\sigma}}\frac{d\bar{\varepsilon}}{d\varepsilon_1} d\varepsilon_1 + \int_{\varepsilon_{1n}}^{\varepsilon_{1f}} \frac{\sigma_m}{\sigma_1}\frac{\sigma_1}{\bar{\sigma}}\frac{d\bar{\varepsilon}}{d\varepsilon_1}\, d\varepsilon_1\right]$$
$$= \frac{1}{\bar{\varepsilon}_f}\frac{1+r}{3}\left[\int_0^{\varepsilon_{1n}} (1+\beta)\, d\varepsilon_1 + \int_{\varepsilon_{1n}}^{\varepsilon_{1f}} (1+\beta_{n-f})\, d\varepsilon_1\right] \tag{10}$$

where r is the normal anisotropy coefficient, β is the slope before necking of a given proportional strain path and β_{n-f} is the slope after necking to fracture, which is assumed to be $\beta_{n-f} \approx 0$. The three partial ratios $d\bar{\varepsilon}/d\varepsilon_1$, σ_m/σ_1 and $\sigma_1/\bar{\sigma}$ are given by

$$\frac{d\bar{\varepsilon}}{d\varepsilon_1} = \frac{(1+r)\sqrt{1+(2r/(1+r))\beta+\beta^2}}{\sqrt{1+2r}} \tag{11}$$

$$\frac{\sigma_m}{\sigma_1} = \frac{1+\alpha}{3} = \frac{(1+2r)(1+\beta)}{3[1+r+r\beta]} \tag{12}$$

$$\frac{\sigma_1}{\bar{\sigma}} = \frac{1}{\sqrt{1+2r}}\frac{[1+r+r\beta]}{\sqrt{1+(2r/(1+r))\beta+\beta^2}} \tag{13}$$

where $\alpha = \sigma_2/\sigma_1$. The derivation of theses partial ratios for Hill's 48 criterion under plane stress conditions can be found elsewhere, see for instance Martins et al. [3].

Rewriting Eq. (9) and (10) as a function of the major and minor strain at the onset of fracture, ε_{1f} and ε_{2f}, the final expresions for $\bar{\varepsilon}_f$ and $\bar{\eta}_f$ are given by

$$\bar{\varepsilon}_f = \frac{1+r}{\sqrt{1+2r}}\left[\varepsilon_{1f} + \left(\sqrt{1+(2r/(1+r))\beta+\beta^2}-1\right)(\varepsilon_{2f}/\beta)\right] \tag{14}$$

$$\bar{\eta}_f = \frac{\sqrt{1+2r}}{3}\left[\frac{\varepsilon_{1f}+\varepsilon_{2f}}{\varepsilon_{1f} + \left(\sqrt{1+(2r/(1+r))\beta+\beta^2}-1\right)(\varepsilon_{2f}/\beta)}\right] \tag{15}$$

where it is assumed that $\varepsilon_{1n} = \varepsilon_{2n}/\beta = \varepsilon_{2f}/\beta$.

Figure 9 shows the mapping of the FFL curve to the $\bar{\varepsilon} - \bar{\eta}$ space according to Eqs. (14) and (15). The strain paths associated to tests in uniaxial tension, plane strain, biaxial strain and equibiaxial strain, highlighted in Figure 5, are also represented for reference. For completeness, the FLC is also depicted. As can be seen, the FLC maintains its typical V-shape. Instead, the FFL shows a sight U-shaped curve, showing a peak at equibiaxial strain. This trend has been experimentally observed in different materials [11,14,25,26]. It is worth noting that, for materials exhibiting linear FFL with large slopes in $\varepsilon_1 - \varepsilon_2$ space, typically near -1, the FFL given by Eqs. (14) and (15) shows a decreasing shape as $\bar{\eta}$ increases in $\bar{\varepsilon} - \bar{\eta}$ space. This evolution has been intensively claimed in various recent publications [3,27].

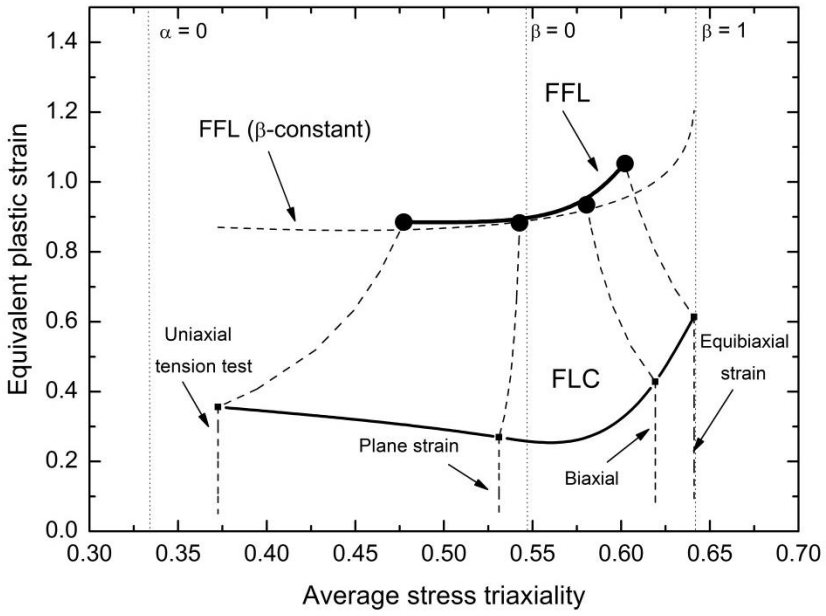

Figure 9. Mapping of the FLC and FFL on the $\bar{\varepsilon} - \bar{\eta}$ space.

According to Figure 9, the average stress triaxiality at fracture for Nakajima tests ranges from 0.48 in uniaxial tension to 0.60 in equibiaxial strain. These values agrees quite well with the numerical results obtained by Bao and Wierzbicki [14] in uniaxial tension tests of AA2024-T351 (round bar), $\bar{\eta}_f \approx 0.4$, and by Mirnia and Shamsari [11] in the uniaxial tension of AA6061-T6 (1mm thickness sheet), $\bar{\eta}_f \approx 0.45$. These values are far from the theoretical 0.33 widely used in literature for pure uniaxial condition of isotropic sheets.

Some recent works devoted to the characterization fracture loci in sheet metal forming by SPIF suggests to map the FFL into $\bar{\varepsilon} - \bar{\eta}$ space by assuming constants strain paths (β-constant) up to fracture in the FLD, arguing the absent of necking in incremental forming [3]. In this case, the integrals of Eqs. (7) and (8) are performed in one step from 0 to $\bar{\varepsilon}_f$, yielding the following expressions:

$$\bar{\varepsilon}_f = \frac{1+r}{\sqrt{1+2r}}\left[\left(\sqrt{1+(2r/(1+r))\beta+\beta^2}\right)\,\varepsilon_{1f}\right] \tag{16}$$

$$\bar{\eta}_f = \frac{\sqrt{1+2r}}{3}\left[\frac{\varepsilon_{1f}+\varepsilon_{2f}}{\left(\sqrt{1+(2r/(1+r))\beta+\beta^2}\right)\varepsilon_{1f}}\right] \tag{17}$$

As can be seen in Figure 9, the FFL expands now significantly, being $\bar{\eta}_f$ ranging from 0.37 to 0.64. The values of $\bar{\varepsilon}_f$ are also slightly modified. The authors would like to draw the attention to this practice, which might cause important misinterpretations of results. In consequence, for metal sheets exhibiting necking, we suggest to use always kinked strain paths to obtain the FFL in $\bar{\varepsilon} - \bar{\eta}$ space.

4.4. Hole-flanging tests by SPIF vs. Nakajima tests in $\bar{\varepsilon} - \bar{\eta}$ space

Figure 10 shows the average stress triaxiality (Eq. 4) in the $\bar{\varepsilon} - \bar{\eta}$ space for the limit flanges obtained by SPIF with ϕ20 mm and ϕ12 mm tool respectively. This is obtained at the element located at fracture site at the outer surface in both flanges. As can be seen, the values of $\bar{\eta}_f$ are around 0.25 in both cases, specifically 0.250 and 0.244 for forming tools of ϕ20 mm and ϕ12 mm respectively. Furthermore, except for the scatter at the beginning of the process, the values of $\bar{\eta}$ during the process are clearly below that value.

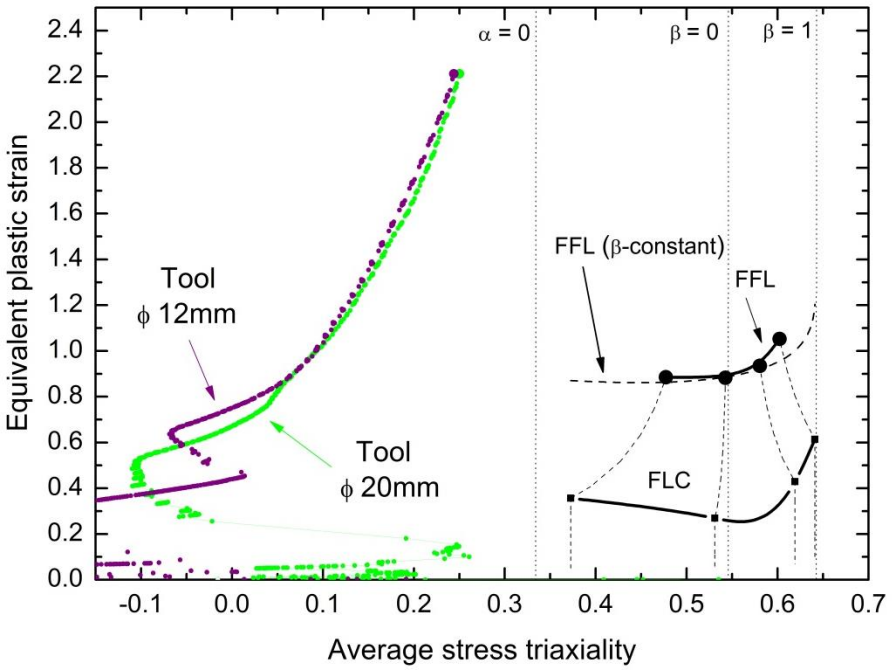

Figure 10. Evolution of the average stress triaxiality at fracture point at the outer surface in the $\bar{\varepsilon} - \bar{\eta}$ space for the limit flanges obtained by SPIF with ϕ20 mm and ϕ12 mm tool respectively. Comparison with the conventional FFL.

The values of $\bar{\eta}_f$ and $\bar{\varepsilon}_f$ in SPIF are clearly different from the ones obtained in Nakajima tests, which contrasts remarkably with what is observed in the $\varepsilon_1 - \varepsilon_2$ space (see Figure 5). In fact, roughly speaking, it can be said that the average stress triaxiality in the SPIF process is less than half the one in the Nakajima tests. As a consequence, it should be expected that the process of microvoid growth develops with more resistance in SPIF than in Nakajima tests, delaying the onset of ductile fracture.

Regarding the level of equivalent plastic strain at fracture, this is around 2.2 in SPIF versus about 0.9 (ranging from 0.88 to 1.05) in Nakajima tests. That is an increase of more than twice due to the incremental forming. This is in fact a consequence of the level of triaxiality, since low values of triaxiality allow accumulating more plastic strain in the material before fracture takes place. This could explain the capability of incremental sheet forming processes to exploit

the ductility of the material in greater extent than conventional forming processes. Therefore, the $\bar{\varepsilon} - \bar{\eta}$ space seems to be an effective tool to explain the improvement of formability observed in SPIF compared to conventional processes.

The above conclusions would support the assumption that microvoid growth phase, a priori the least favored mechanism, controls the onset of ductile fracture in incremental sheet forming processes. As mentioned before, this hypothesis has been widely used in literature and indirectly corroborated with many experimental FFL obtained by SPIF, which exhibit a slope near to -1 in the $\varepsilon_1 - \varepsilon_2$ space [27,28]. However, this hypothesis is less clear in Nakajima tests, where not only microvoid growth but also microvoid coalescence play an important role to trigger ductile fracture. This is macroscopically observed by conventional FFL, i.e. obtained by Nakajima tests, with slopes different to -1, typically below [7,10,29,30].

According to the present analysis, the FFL curves in incremental sheet forming and in conventional forming are in principle different fracture loci, and such differences can be explained by the significant differences in average stress triaxiality in both deformation processes. This agrees with the results pointed out recently by Mirnia and Shamsari in AA6061-T6 [11]. They attributed such differences to the highly nonlinear loading induced in the material by SPIF, which, as shown in the present work, affects notably to triaxiality. Only when the phase of micro-void growth absolutely dominates over the nucleation and coalescence of micro-voids in both the incremental and conventional deformation process, the two fracture loci would coincide.

5. Conclusions

In this work a critical study of the evolution of stress triaxiality in hole flanging by single-stage SPIF is presented. A numerical model of the flanging process is developed using the software LS-Dyna for ANSYS™. The influence of stress triaxiality on the material formability in SPIF tests is discussed and compared with conventional Nakajima tests in the $\bar{\varepsilon} - \bar{\eta}$ space. The material analyzed is AA7075-O in sheets of 1.6 mm thickness. The main conclusions are summarized as follow:

- The local evolution of stress triaxiality at fracture point at the outer and inner side of the flange shows an oscillating pattern due to the successive passages of the tool. The value varies from 0.66 to -0.66, which are related with an alternating local strain ratio (β) ranging from near equibiaxial stretching to near equibiaxial compression.
- The equivalent plastic strain at fracture point increases stepwise up to fracture at both surfaces, remaining constant when the tool is far from this point indicating that only elastic deformation takes place. During these periods, the local stress triaxiality remains also in the elastic regime, presumably without increasing damage in the material.

- The average stress triaxiality ($\bar{\eta}_f$) and the equivalent plastic strain ($\bar{\varepsilon}_f$) to fracture are higher at the outer surface than at the inner one, suggesting that the outer surface exhibits less resistance to accumulate damage by micro-void growth. As a result, the fracture in SPIF initiates likely at this side.
- The analytical procedure of mapping the FFL from the $\varepsilon_1 - \varepsilon_2$ space to the $\bar{\varepsilon} - \bar{\eta}$ space, using the kinked strain path associated to the onset of local necking in Nakajima tests, is presented. The average stress triaxiality at fracture ranges from 0.48 in uniaxial tension tests to 0.60 in equibiaxial strain tests, which is in good agreement with other investigations.
- The values of the average stress triaxiality and the equivalent plastic strain at fracture in SPIF are clearly different from the ones obtained in Nakajima tests. In general terms, $\bar{\eta}_f$ in SPIF is less than half that in Nakajima tests, and $\bar{\varepsilon}_f$ more than double that in such tests.
- These differences seem to explain the enhancement on formability exhibited by SPIF respect to Nakajima tests. Furthermore, they may lead to significant differences in the fracture process, suggesting that FFL curves in incremental sheet forming and in conventional forming are in general different curves.

Finally, it should be noted that the behavior described here should be dependent on the type of material (microstructure, heat treatment, etc.). So an intensive study with different materials should be done before establishing more general conclusions.

Acknowledgments: The authors wish to thank the Spanish Ministry of Education for its financial support throughout the major grant DPI2015-64047-R. The collaboration of MSc Alberto Caballero is greatly acknowledged.

References

[1] Jeswiet, J., Micari, F., G. Hirt, A. Bramley, J. Duflou, J. Allwood. Asymmetric single point incremental forming of sheet metal. CIRP Ann. Manuf. Technol. 54(2), 88–114, 2005.

[2] Silva M. B., Nielsen P.S., Bay N., Martins, P.A.F. Failure mechanisms in single-point incremental forming of metals, The International Journal of Advanced Manufacturing Technology, 56, 893–903, 2011.

[3] P.A.F. Martins, N. Bay, A.E. Tekkaya, A.G. Atkins. Characterization of fracture loci in metal forming. International Journal of Mechanical Sciences. Int. Journal of Mechanical Sciences 83, 112-123, 2014.

[4] Madeira, T., Silva, C.M.A., Silva, M.B., Martins, P.A.F., Failure in single point incremental forming, Int J. Adv Manuf Technol 80: 1471- 1479, 2015.

[5] Silva M. B., Teixeira P., Reis, A., Martins, P.A.F., On the formability of hole-flanging by incremental sheet forming, Proc IMechE Part L: J Materials: Design and Applications 227(2) 91–99, 2013.

[6] Cristino, V.A.M., Silva, M.B., Wong, P.K., Tam, L.M., Martins, P.A.F., Hole-flanging of metals and polymers produced by single point incremental forming, International Journal of Materials and Product Technology 50, 37-48, 2015.

[7] Centeno, G., Bagudanch, I., Martínez-Donaire, A.J., Garcia-Romeu, M.L., Vallellano, C. Critical analysis of necking and fracture limit strains and forming forces in single-point incremental forming. Mater. Des. 63, 20–29, 2014.

[8] Centeno, G.; Martínez-Donaire, A.J.; Bagudanch, I.; Morales-Palma, D.; Garcia-Romeu, M.L.; Vallellano, C., Revisiting Formability and Failure of AISI304 Sheets in SPIF: Experimental Approach and Numerical Validation, Metals 7, 531, 2017

[9] Haque, M.Z. and Yoon, J.W. Stress based prediction of formability and failure in incremental sheet forming, Int. J. Mater. Form. 9, 413–421, 2016.

[10] Borrego M., Morales-Palma D., Martínez-Donaire A.J., Centeno G., Vallellano C., Experimental study of hole-flanging by single-stage incremental sheet forming, Journal of Materials Processing Technology, 237, 320-330, 2016.

[11] Mirnia, M.J., Shamsari, M., Numerical prediction of failure in single point incremental forming using a phenomenological ductile fracture criterion, J. of Mater. Processing Technology 244, 17–43, 2017.

[12] McClintock, F.A., A criterion for ductile fracture by the growth of holes, J. Appl. Mech. – Trans. ASME 35, 363–371, 1698.

[13] Rice, J.R., Tracey, D.M., On the ductile enlargement of voids in triaxial stress fields, Journal of the Mechanics and Physics of Solids 17, pp. 201–217, 1969.

[14] Bao, Y, Wierzbicki, T., On fracture locus in the equivalent strain and stress triaxiality space, International Journal of Mechanical Sciences 46, 81–98, 2004.

[15] Wierzbicki, T., Bao, Y., Lee, Y.W., Bai, Y., Calibration and evaluation of seven fracture models, Int J Mech Sciences 47, pp. 719-743, 2005.

[16] Lou, Y., Huh, H., Lim, S., Pack, K., New ductile fracture criterion for prediction of fracture forming limit diagrams of sheet metals, Int. J. of Solids and Structures 49, pp. 3605–3615, 2012.

[17] Gatea, S., Ou, H., Lu, B., McCartney, G., Modelling of ductile fracture in single point incremental forming using a modified GTN model, Engineering Fracture Mechanics 186, pp.59–79, 2017.

[18] Barlat, F., Lian, K., Plastic behavior and stretchability of sheet metals. Part I: A yield function for orthotropic sheets under plane stress conditions. Int. Journal of Plasticity 5 (1), 51–66, 1989.

[19] Y. Fang, B. Lu, J. Chen, D.K. Xu, H. Ou. Analytical and experimental investigations on deformation mechanism and fracture behavior in single point incremental forming, Journal of Materials Proc. Tech. 214 (8), 1503-1515, 2014.

[20] Morales-Palma, D.; Vallellano, C.; García-Lomas, F.J. Assessment of the effect of the through-thickness strain/stress gradient on the formability of stretch-bend metal sheets, Mater. Des., 50, 798–809, 2013.

[21] Morales-Palma, D.; Martínez-Donaire, A.J.; Vallellano, C., On the Use of Maximum Force Criteria to Predict Localised Necking in Metal Sheets under Stretch-Bending, Metals, 7, 469, 2017.

[22] Seong, D.Y., Haque, M.Z., Kim, J.B., Stoughton, T.B., Yoon, J.W., Suppression of necking in incremental sheet forming. Int. J. Solids Struct. 51, 2840–2849, 2014.

[23] Atkins, A.G., Fracture in forming, J. Mater. Process. Technol. 56, 609–618, 1996.

[24] Sheng, Z.Q., Mallick, P.K., A ductile failure criterion for predicting sheet metal forming limit, International Journal of Mechanical Sciences 128–129, 345-360, 2017.

[25] Bai, Y., Wierzbicki, T., A comparative study of three groups of ductile fracture loci in the 3D space. Eng. Fract. Mech. 135, 147–167, 2015.

[26] Li, Y., Wierzbicki, T., Prediction of plane strain fracture of AHSS sheets with post-initiation softening, International Journal of Solids and Structures 47, 2316-2327, 2010.

[27] Soeiro J.M.C., Silva C.M.A., Silva, M.B. and Martins, P.A.F. Revisiting the formability limits by fracture in sheet metal forming. Journal of Material Processing Technology 217, 184-192, 2015.

[28] Do, V.C., Pham, Q.T., Kim, Y.S., Identification of forming limit curve at fracture in incremental sheet forming, Int J Adv Manuf Technol 92, 4445-4455, 2017.

[29] Isik, K., Silva, M.B., Tekkaya, A.E., Martins, P.A.F., Formability limits by fracture in sheet metal forming, Journal of Materials Processing Technology 214, 1557-1565, 2014.

[30] Heibel, S., Nester, W., Clausmeyer, T., Tekkaya, A.E., Failure assessment in sheet metal forming using a phenomenological damage model and fracture criterion: experiments, parameter identification and validation, Procedia Engineering 207, 2066-2071, 2017.